J. Phys. D: Appl. Phys. **42** (2009) 045210 (11pp) doi:10.1088/0022-3727/42/4/045210

Investigating near-anode plasma layers of very high-pressure arc discharges

N A Almeida[1], M S Benilov[1], U Hechtfischer[2] and G V Naidis[3]

1 Departamento de Física, Universidade da Madeira, 9000 Funchal, Portugal
[2] Philips Research Laboratories, 52066 Aachen, Germany
[3] Joint Institute for High Temperatures of the Russian Academy of Sciences, Moscow 125412, Russia

Received 17 November 2008, in final form 21 December 2008
Published 28 January 2009
Online at stacks.iop.org/JPhysD/42/045210

Abstract
Numerical and experimental investigation of near-anode layers of very high-pressure arcs in mercury and xenon is reported. The simulation is performed by means of a recently developed numerical model in which the whole of a near-electrode layer is simulated in the framework of a single set of equations without simplifying assumptions such as thermal equilibrium, ionization equilibrium and quasi-neutrality and which was used previously for a simulation of the near-cathode plasma layers. The simulation results support the general understanding of similarities and differences between plasma–cathode and plasma–anode interaction in high-pressure arc discharges established in preceding works. In particular, the anode power input is governed primarily by, and is approximately proportional to, the arc current. In the experiment, the spectral radiance from the electrodes and the near-electrode regions in xenon arcs was recorded. The derived total anode power input and near-anode plasma radiance distribution agree reasonably well with the simulation results.

(Some figures in this article are in colour only in the electronic version)

1. Introduction

The plasma–electrode interaction in high-pressure arc discharges is dominated by non-LTE effects (e.g. [1] and references therein), which include a violation of thermal equilibrium, i.e. a divergence between the electron and heavy-particle temperatures, a violation of ionization equilibrium, i.e. a deviation of the charged-particle density from that predicted by the Saha equation, and a violation of quasi-neutrality, i.e. a divergence between the electron and ion number densities. A straightforward numerical calculation of near-electrode plasma layers with an account of all these effects represents a difficult task. Therefore, in most works either some of these effects are discarded (e.g. [2–7]) or the near-electrode layer is *a priori* divided into a number of sub-layers, such as a layer of thermal non-equilibrium, an ionization layer, a near-electrode space-charge sheath, etc, with each sub-layer being described by a separate set of equations and solutions in adjacent sub-layers being matched in some way or other at a boundary between the sub-layers (e.g. [1] and references therein).

Papers in which the whole of a near-electrode layer is simulated in the framework of a single set of equations with account of all the above-mentioned non-LTE effects have started to appear only recently [8, 9]. Such a unified modelling approach does not rely on intuitive considerations, which are inevitable in models based on sub-layers and differ from one model to another, and is useful for developing commonly accepted physical understanding and/or simulation methods. This approach is independent of polarity and allows one to model both near-cathode and near-anode layers by means of the same code by merely changing the sign of the current density, a feature important from the methodical point of view and essential for modelling near-electrode layers of ac arcs.

In this work, the numerical model [9], which was used previously for a simulation of near-cathode plasma layers, is employed for the investigation of near-anode layers of very high-pressure arcs in mercury and xenon. Note that the use of arc discharges with pressures of 100 bar and higher was the key to the development of exceptionally compact and bright light sources which are required for, e.g., digital projection. Physics of very high-pressure arc discharges is diverse and complex and not all aspects of it are well understood. In particular, there are open questions concerning arc–electrode interaction. There are a variety of methods of experimental investigation of interaction of high-pressure arcs with electrodes; see, for example, reviews [10, 11] and references therein. Unfortunately, most of these methods cannot be applied under conditions of very high-pressure arcs and the only viable diagnostic means in most cases is the analysis of radiation emitted by the electrodes (pyrometry) and the near-electrode regions of the arc (plasma spectroscopy). Numerical modelling is of primary importance in this situation. Note that simulations of near-anode layers in high-pressure arc discharges reported previously [8, 12–14] refer to strongly different conditions (argon arcs under pressures of 1 bar [12–14] and 2.6 bar [8]); besides, the simulations [12–14] were performed in the quasi-neutral approximation, i.e. neglecting the charge separation.

Very little experimental information has been published up to now on electrodes of very high-pressure arc discharges. Therefore, we performed special experiments in order to get at least some basic quantitative data on the plasma–anode interaction in very high-pressure arcs in xenon, which could be compared with the theory. We measured the radiance of the electrodes and the near-electrode plasma in an experimental very high-pressure xenon lamp and determined the temperature of the electrodes and the total power received by the electrodes from the plasma. The derived total anode power input and near-anode plasma radiance distribution agree reasonably well with predictions of the theoretical model.

2. Theory

The simulations have been performed by means of the model [9]. The model takes into account the neutral atoms, ions and electrons; the atoms and ions have the same temperature T_h which is in general different from the electron temperature T_e. The system of equations includes equations of conservation of each species, transport equations for each species, equation of energy of the heavy species (the atoms and ions), equation of energy of the electrons and the Poisson equation. The transport equations for species are written in the form of hydrodynamic Stefan–Maxwell equations (e.g. [15, 16] and references therein), which take into account the multicomponent diffusion and are therefore applicable at any ionization degree of the plasma, in contrast to a description based on Fick's law for the ions and the electrons which is valid provided that the ionization degree is low enough.

2.1. Modelling parallel-plane current transfer

The modelling results reported in this work refer to the case of parallel-plane current transfer to a planar electrode through a planar near-electrode region, the case which is different from the case of spherically symmetric current transfer to a hemispherical electrode through a spherically symmetric near-electrode region treated in [9]. The system of governing ordinary differential equations for the planar case is obtained from the system formulated in [9] by setting $B = 1$ and replacing equation (21) with

$$p = p_0 + \varepsilon_0 \frac{E^2 - E_0^2}{2}, \tag{1}$$

where p and E are the local plasma pressure and electric field and p_0 and E_0 are the plasma pressure and electric field at a reference point. Note that the second term on the right-hand side of this equation is minor in near-anode layers; however, it is comparable to the first term in the near-cathode space-charge sheath at high current densities and therefore should be retained. The independent variable is x the distance from the electrode surface. The current density j is the same at all points of the plasma in the planar case and is considered as an input parameter. Note that the positive direction for the electric field and the current density is that from the electrode into the plasma; that is, E and j represent projections of the corresponding vectors over the x-axis.

The boundary conditions at the electrode surface, $x = 0$, are the same as in [9] and take into account the emission of electrons by the surface. Since the current density is constant in the planar geometry, all parameters of the plasma (except for the electrostatic potential) are constant at large distances from the electrode, where the plasma is close to the state of local thermodynamic equilibrium, or LTE, and its energy balance is dominated by radiation. One can say that the plasma far from the electrode is not disturbed by the electrode. The upper boundary of the calculation domain, $x = L$, in the planar case is positioned in the undisturbed plasma and the conditions at this boundary are zero derivatives:

$$\frac{\mathrm{d}n_e}{\mathrm{d}x} = \frac{\mathrm{d}E}{\mathrm{d}x} = \frac{\mathrm{d}T_e}{\mathrm{d}x} = \frac{\mathrm{d}T_h}{\mathrm{d}x} = 0. \tag{2}$$

Here n_e is the number density of the electrons. Note that these boundary conditions, while being applied in a uniform plasma, are equivalent to the boundary conditions which were used in [9] and amount to assuming that the plasma at $x = L$ is close to LTE and its energy balance is dominated by radiation.

The reference point in equation (1) is naturally identified with the upper boundary of the calculation domain, then p_0 represents the plasma pressure at $x = L$, i.e. in the undisturbed plasma.

One of the most important parameters characterizing plasma–electrode interaction is the voltage drop in the near-electrode perturbation region, which is also referred to as the near-electrode voltage drop or the near-electrode voltage. This parameter may be evaluated with the use of the modelling results after the problem has been solved, provided that an appropriate definition of the near-electrode voltage drop is adopted. In the planar case, the voltage drop in the near-electrode perturbation region may be defined in a natural and unambiguous way as follows. The distribution of the electrostatic potential in the undisturbed plasma is linear. Let us extrapolate this distribution down to the electrode surface. The deviation between this extrapolated value and the actual potential of the electrode surface, shown in figure 1, characterizes a perturbation introduced by the electrode and may be called the near-electrode voltage drop. It should be stressed that this definition does not rely on the concept of an 'edge' of the near-electrode layer, which cannot be chosen in an unambiguous way, and conforms to the way in which the near-electrode voltage drops in high-pressure arc discharges are determined by means of electrostatic probe measurements [17]. The sign in the definition of the near-electrode voltage shown in figure 1 depends on the polarity, in agreement with

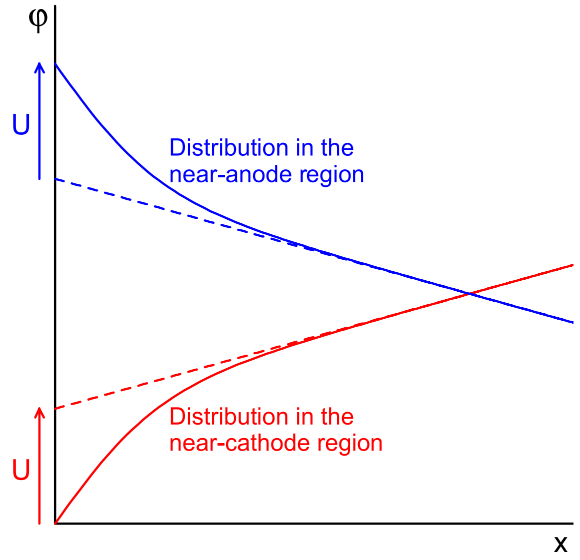

Figure 1. Solid: schematics of distributions of the electrostatic potential in the near-cathode and near-anode regions. Dashed: distributions of electrostatic potential in the undisturbed plasma.

the usual sign convention for the near-electrode voltage: if the electric field in the near-electrode layer is higher than and has the same direction as the electric field in the undisturbed plasma, then the near-electrode voltage is positive. The near-electrode layer consumes more electrical power than a layer 'of the same thickness' in the undisturbed plasma in the case $U > 0$ and less power in the case $U < 0$.

A formula expressing the definition of the near-electrode voltage drop shown in figure 1 may be obtained as follows. The distribution of the potential in the undisturbed plasma is described by the linear function $C - E_\infty x$, where $C = \lim_{x\to\infty}[\varphi(x) + E_\infty x]$. (The index ∞ is attributed to values of corresponding quantities in the undisturbed plasma.) Then the above definition may be expressed as

$$U = \pm\left\{\lim_{x\to\infty}[\varphi(x) + E_\infty x] - \varphi(0)\right\} \tag{3}$$

or, equivalently,

$$U = \pm\int_0^\infty (E_\infty - E)\,\mathrm{d}x. \tag{4}$$

Here and later, the upper and lower signs refer to, respectively, the cathode and the anode.

It will be convenient for analysis of numerical results to introduce the difference between the potential in the near-anode layer, $\varphi(x)$, and the function $\varphi(0) - E_\infty x$:

$$u(x) = \varphi(x) - \varphi(0) + E_\infty x. \tag{5}$$

$\varphi(0) - E_\infty x$ may be viewed as the distribution of potential which would prevail if the near-electrode layer were absent. Therefore, function $u(x)$ represents the perturbation of the electrostatic potential caused by the presence of the near-electrode layer. This function is related to the near-electrode voltage drop by the formula $U = \pm\lim_{x\to\infty} u(x)$.

In the numerical calculations, U is evaluated as

$$U = \pm[\varphi(L) - \varphi(0) + E_\infty L]. \tag{6}$$

The energy balance of the near-electrode layer may be expressed in terms of U as follows. Applying equations (37) and (38) of [9] to the near-electrode layer limited by a coordinate x positioned in the undisturbed plasma, one can obtain the equation of conservation of energy of the layer in the following form:

$$q_w = \frac{j}{e}\left[\left(\frac{5}{2} + \xi_{e\infty}\right)kT_{e\infty} + A_f\right] + j[\varphi(0) - \varphi(x)] - \int_0^x w_{\mathrm{rad}}\,\mathrm{d}x. \tag{7}$$

Here q_w is the density of energy flux from the near-electrode layer to the electrode surface, $\xi_{e\infty}$ is the value in the undisturbed plasma of a kinetic coefficient ξ_e which describes the effect inverse to the thermal diffusion of electrons and is expressed as $\xi_e = A_i^{(e)} + A_a^{(e)}$, where $A_i^{(e)}$ and $A_a^{(e)}$ are coefficients defined in [9], A_f is the work function of the electrode material and w_{rad} is the density of losses of energy of the plasma inside the layer through radiation. Note that the terms on the right-hand side represent, respectively, the density of energy flux transported by the electron current to the near-electrode layer from the undisturbed plasma (with the ion current neglected), the electrical power supplied to the layer and the radiated power. Since this equation applies to a thin near-electrode layer, it is written in one dimension and bears no account of losses of energy in directions along the electrode.

Rearranging the second and third terms on the right-hand side of equation (7) with the use of equality $jE_\infty = w_{\mathrm{rad}\infty}$, applying the limit $x \to \infty$ and making use of equation (3), one can rewrite equation (7) as

$$q_w = \frac{j}{e}\left[\left(\frac{5}{2} + \xi_{e\infty}\right)kT_{e\infty} + A_f\right] \mp jU - \Delta W_{\mathrm{rad}}, \tag{8}$$

where ΔW_{rad} represents the difference between the power radiated by the near-electrode perturbation layer and a layer 'of the same thickness' in the undisturbed plasma,

$$\Delta W_{\mathrm{rad}} = \int_0^\infty (w_{\mathrm{rad}} - w_{\mathrm{rad}\infty})\,\mathrm{d}x. \tag{9}$$

Note that equations of integral balance of energy of near-electrode layers, similar to equation (8), have been well known since the work [18].

Introducing the so-called electrode heating voltage $U_h = q_w/|j|$, one can rewrite equation (8) as

$$U_h = \mp\left[\left(\frac{5}{2} + \xi_{e\infty}\right)kT_{e\infty} + A_f\right]\frac{1}{e} + U - \Delta U_{\mathrm{rad}}, \tag{10}$$

where $\Delta U_{\mathrm{rad}} = \Delta W_{\mathrm{rad}}/|j|$.

2.2. Transport, kinetic and radiation coefficients of the xenon plasma

The results reported in this paper refer to cases where the plasma-producing gas is Hg or Xe. Transport, kinetic and

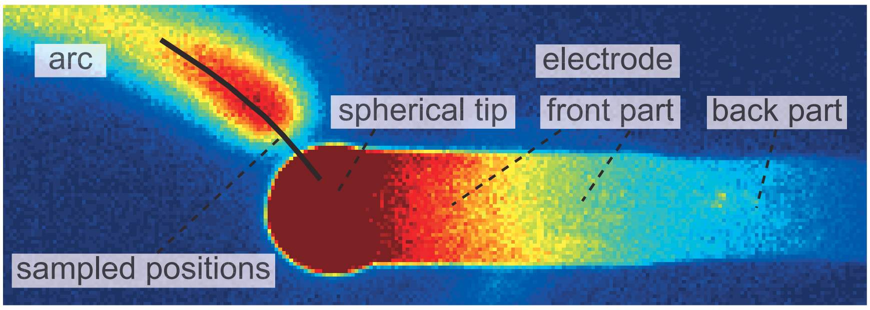

Figure 2. Typical CCD image of one electrode in the experimental very high-pressure Xe lamp, when operated as the anode at 0.5 A. The curved line indicates the locations for sampling the arc-centre plasma radiance data given in figure 7. Additional sample points on the electrode were used for reference.

radiation coefficients for the Hg plasma are described in [9]. The coefficients for the Xe plasma were evaluated as described in [9] with the following modifications. The average cross section $\bar{Q}_{ia}^{(1,1)}$ of ion–atom collisions was evaluated by means of the analytical formula [19] with coefficients obtained by an approximation of the resonant charge exchange cross section from [20] (these data can also be found in [21]). The energy-dependent cross section for momentum transfer in collisions electron–atom, $Q_{ea}^{(1)}(\varepsilon)$, was taken from [22, 23]. The average cross sections $\bar{Q}_{aa}^{(2,2)}$ and $\bar{Q}_{ia}^{(2,2)}$ were evaluated by means of the formulae $\bar{Q}_{aa}^{(2,2)} = 1.85 \times 10^{-18} T_h^{-0.2}$, $\bar{Q}_{ia}^{(2,2)} = 6.1 \times 10^{-18} T_h^{-0.3}$ (here T_h is in K and $\bar{Q}_{ia}^{(2,2)}$ in m^2), which were obtained as described in [9] with the use of the data from [24] and, respectively, [21].

The rate constant of direct ionization of the xenon atoms is evaluated with the use of the Maxwellian electron energy distribution function and the derivative of the ionization cross section taken from [25] with respect to the electron energy, evaluated at the threshold. The value $n_e^{(0)}$ of the electron density at which the decrease of the rate of stepwise ionization due to radiation escape comes into play was estimated for xenon in the same way as in [9] for argon and mercury and was found equal to 3×10^{20} m^{-3}. The radiation energy losses were evaluated, similarly to [9], by means of an interpolation between an LTE value and a value obtained by assuming that the de-excitation of the radiating atomic state due to radiation escape prevails over the de-excitation in collisions with electrons. The former (LTE) value was estimated by means of the formula

$$w_{rad} = 1.8 \times 10^{24} \frac{p}{T_e^{2.5}} \exp\left(-\frac{1.19 \times 10^5}{T_e}\right) \qquad (11)$$

(here p is in bar, T_e in K, w_{rad} in W m^{-3}). This formula was obtained by fitting the data [26] taking into account the fact that the net emission coefficient is approximately proportional to the plasma pressure.

3. Experimental

The very high-pressure xenon test lamp used in the experiment was in principle a normal Philips mercury-free xenon automotive headlamp (XenEco) with a rated power of 35 W, but filled with only Xe (at a cold pressure of approximately 15 bar), i.e. without the normal metal-halide salt fill. The quartz discharge vessel had an inner diameter and volume of 2.4 mm and 20 mm^3, respectively. The inter-electrode distance was about 3.6 mm. The electrodes were pure-tungsten rods with a diameter of 0.34 mm at the front part (up to 1.10 mm from the tip) and 0.30 mm at the back part. Near the tip, the cylindrical front should have molted into a sphere of diameter 0.39 mm. A similar electrode is shown in figure 2. The free length (from the tip to the contact with the quartz feedthrough) was approximately 2.0 mm.

For the measurements, the lamp was operated horizontally on a programmable current source and imaged with a CCD camera through a narrow 850 nm bandpass filter. That wavelength had been chosen to minimize the signal from the Xe plasma when detecting the Planck radiation from the electrodes. The measured images were translated to absolute spectral radiance based on a calibration with a tungsten-ribbon lamp. The image in figure 2 is an example. Note that the 'pixel' character of the image is not due to a bad graphics handling; what is seen in the figure are the real pixels of the CCD camera.

In order to record in a single experiment the radiance images of both electrodes when operating as a dc cathode and an anode at different currents, the lamp was ignited, allowed to stabilize for a minute during normal ac operation and then taken through a pre-programmed, randomized current pattern with currents I between 0.4 and 1.7 A, for both polarities. Each current was held for 1 s, long enough for the electrodes (which are small enough) to reach quasi-dc steady-state temperature profiles. This situation was recorded by CCD images which were taken periodically every second, near the end of the intervals of constant current.

From the resulting spectral-radiance data, we extracted the axial surface temperature profiles of the electrodes as usual by inverting the Planck law and including the temperature-dependent emissivity of tungsten [27] as well as the small reflection losses at the inner and outer bulbs. The estimated uncertainty of the derived temperatures is about 50 K.

The axial temperature profiles were mapped linearly to positions on the electrode. Slightly different pixel-to-mm magnifications had to be assumed radially and axially, to account for the optical distortion by the bulb in the axial direction; the axial magnification was determined from the known position of the electrode-diameter step. The resulting profiles were then fitted by a theoretical temperature profile

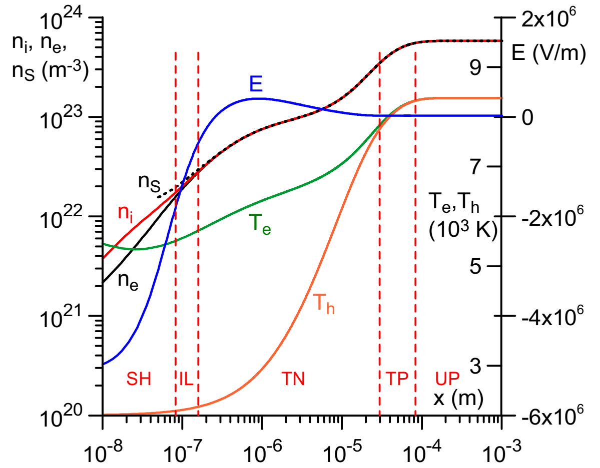

Figure 3. Distribution of parameters in the near-anode layer of the Hg plasma. $p_0 = 100$ bar, $T_w = 2000$ K, $j = 10^7$ A m^{-2}. UP: the region of undisturbed plasma. TP: the layer of thermal perturbation. TN: the layer of thermal non-equilibrium. IL: the ionization layer. SH: the space-charge sheath.

from a finite-difference thermal model of the electrode. The free parameters were P_{in}, the power input injected by the plasma into the electrode tip, and T_{foot}, the temperature at 2.0 mm from the tip. The power input P_{in} is mainly related to the gradient of the axial temperature profile. This approach yielded for each setting (anode or cathode, $I = 0.4, \ldots, 1.7$ A) the dc power input and foot temperature of the electrodes.

4. Results and discussion

4.1. Theoretical results

A typical calculated distribution of the charged-particle densities, electron and heavy-particle temperatures and electric field in the near-anode layer is shown in figure 3. This distribution refers to the Hg plasma, the pressure in the undisturbed plasma $p_0 = 100$ bar, the temperature of the anode surface $T_w = 2000$ K and the current density $j = 10^7$ A m^{-2}. The electrode in this and all the following simulations is assumed to be made of pure tungsten, n_i is the number density of the ions, n_S is the charged-particle density evaluated by means of the Saha equation in terms of the local heavy-particle and electron temperatures T_h and T_e and the local plasma pressure equal to the pressure in the undisturbed plasma, $p = p_0$.

There is a region of undisturbed plasma with constant parameters in figure 3 at $x \gtrsim 100\,\mu$m. This region represents an analogue of the zone designated in the near-cathode simulations [9] the region of radiation-dominated LTE plasma; the difference is that parameters in the radiation-dominated LTE plasma under conditions of the modelling [9] are non-uniform due to a variable current density which originates in the spherical geometry. The layer separating the undisturbed plasma from the anode, in which deviations from LTE and the equilibrium between Joule heating and radiation are localized, will be referred to as the near-anode non-equilibrium layer. This layer may be divided into four zones. In an (outer) zone that borders the undisturbed plasma the balance between Joule heating and radiation cooling is perturbed by the cooling effect of the anode, so the plasma parameters are not spatially uniform anymore. In this zone, quasi-neutrality holds, $n_e \approx n_i$, ionization (Saha) equilibrium holds, $n_e \approx n_S$, and thermal equilibrium holds, $T_e \approx T_h$. Since the description of the plasma employed in [9] and in this work does not involve the population of excited states, these three kinds of equilibrium jointly amount to the local thermodynamic equilibrium of the plasma. This is the same zone that was designated in [9] the layer of thermal perturbation. Note that this layer represents a part of the near-anode non-equilibrium layer and in this sense it would be natural to term it 'sub-layer'; however for simplicity we retain the term 'layer'. Closer to the anode surface, T_e deviates from T_h and starts decreasing more slowly than T_h does: thermal equilibrium breaks down, and so does LTE on the whole. But ionization equilibrium and quasi-neutrality still prevail. This zone was designated in [9] the layer of thermal non-equilibrium. Still closer to the anode surface, n_i and n_e deviate from n_S: ionization equilibrium breaks down, while quasi-neutrality still prevails. This zone was designated in [9] the ionization layer. Finally, n_i deviates from n_e: quasi-neutrality breaks down. This is the space-charge sheath.

The above-described structure of the near-anode perturbation region is schematically shown in figure 3 by the vertical dashed lines. It is similar to the structure of the near-anode region in high-current arcs proposed in [28, 29] and to the structure of the near-cathode region found in the unified modelling of near-cathode layers [9].

One can see that the quasi-neutrality under conditions of figure 3 breaks down shortly after the ionization equilibrium, i.e. the ionization layer is thin and not very well pronounced. The same feature was found in [9] for the near-cathode layer of a very high-pressure mercury plasma. The near-anode space-charge sheath under conditions of figure 3 also is pronounced rather poorly: the densities of the charged particles differ by no more than a factor of 2. This is contrary to what happens in the near-cathode layer under conditions of practical interest. The ion density n_i in the sheath exceeds the electron density n_e and the electric field in the sheath and the ionization layer is negative, i.e. directed to the electrode surface. This situation is typical for near-cathode layers but occurs frequently also in near-anode layers, namely, in cases where the electron density in the near anode plasma is higher than that needed to provide transport of the arc current to the anode and a part of the plasma electrons must be prevented from entering the sheath, see, for example, the discussion and references in [30] and the estimates in [1].

The electrostatic potential $\varphi(x)$ for conditions of figure 3 is depicted by the solid line 1 in figure 4. (Zero of potential is chosen at the surface of the electrode.) The dashed lines in this figure depict the function $u(x)$, which represents the perturbation of the electrostatic potential due to the presence of the near-anode layer (section 2.1). The voltage drop across the space-charge sheath and the ionization layer is negative (we recall the convention of sign of the near-electrode voltage mentioned in section 2.1) in accordance with the sign of the local electric field and amounts to approximately −0.4 V.

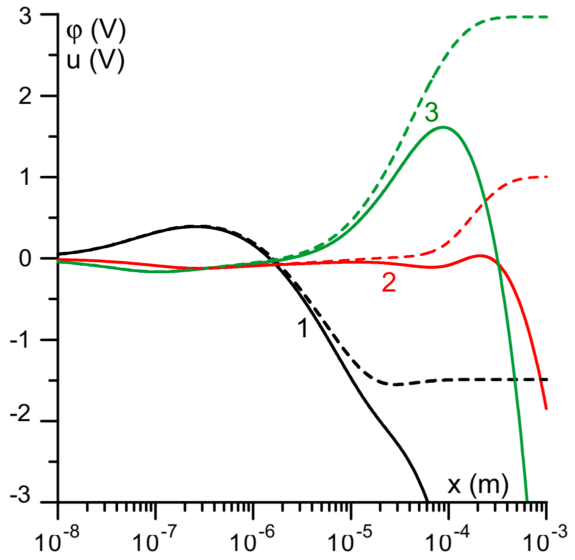

Figure 4. Solid: electrostatic potential in the near-anode layer. Dashed: perturbation of the electrostatic potential due to the presence of the near-anode layer. $p_0 = 100$ bar, $T_w = 2000$ K. 1: Hg plasma, $j = 10^7$ A m^{-2}. 2: Xe plasma, $j = 10^7$ A m^{-2}. 3: Xe plasma, $j = 10^8$ A m^{-2}.

However, the sheath and the ionization layer are rather thin while the electric field in the layers of thermal non-equilibrium and thermal perturbation is positive and exceeds E_∞, which is why the total near-anode voltage is positive (1.49 V).

Distributions of the charged-particle densities, electron and heavy-particle temperatures and the electric field calculated for the Xe plasma, $p_0 = 100$ bar, two values of the temperature of the anode surface, $T_w = 2000$ K and $T_w = 3500$ K and two values of the current density, $j = 10^7$ A m^{-2} and $j = 10^8$ A m^{-2}, are shown in figure 5. Distributions of the electrostatic potential and the perturbation of the electrostatic potential due to the presence of the near-anode layer for two of the variants are depicted by the lines 2 and 3 in figure 4. Comparing the distributions for similar conditions for the mercury and xenon plasmas (figures 3 and 5(*a*), lines 1 and 2 in figure 4), one can note the following differences. The thickness of the near-anode non-equilibrium layer in xenon is larger than in mercury. The ionization layer in xenon is also somewhat thicker than in mercury. The space-charge sheath in xenon is thicker as well and is much better pronounced, n_e in the sheath exceeds n_i and the electric field in the sheath is positive. However, absolute values of electric field in the near-anode layer in xenon are lower than in mercury, which is why the variation of the potential in the region $x \lesssim 10^{-4}$ m, comprising the sheath and the ionization and thermal non-equilibrium layers, is quite small and the dominating contribution to the total near-anode voltage is given by the layer of thermal perturbation. Since the electric field in the layer of thermal perturbation in xenon is below E_∞, the near-anode voltage is negative (-1.00 V). In other words, the near-anode layer consumes more electrical power than a layer 'of the same thickness' in the undisturbed plasma in the case of mercury and less power in the case of xenon.

Comparing distributions shown in figures 5(*a*)–(*d*), one concludes that the effect of the temperature of the anode surface on the distributions of parameters in the near-anode layer is rather weak. The increase in the current density produces a more pronounced effect, especially on densities of the charged particles.

As the distance x to the anode surface decreases, the electron temperature T_e shown in figures 3 and 5 decreases in the outer part of the near-anode non-equilibrium layer and shows a non-monotonic behaviour inside the space-charge sheath and in its proximity. However, variations of T_e in the sheath are rather small. This is contrary to a pronounced maximum of T_e that occurs under conditions of practical interest inside the near-cathode space-charge sheath [9] and is a manifestation of a strong supply of energy to the electron gas in the space-charge sheath that makes possible the generation of an ion current necessary to compensate the deficit of the electron current.

Parameters of the near-anode non-equilibrium layers are summarized in table 1: the electron temperature at the anode surface and in the undisturbed plasma, T_{ew} and $T_{e\infty}$; the value $\xi_{e\infty}$ in the undisturbed plasma of the kinetic coefficient which describes the effect inverse to the thermal diffusion of electrons, the voltage drop U in the near-anode non-equilibrium layer, the anode heating voltage $U_h = q_w/j$ and ΔU_{rad} the voltage equivalent of the difference between the power radiated by the near-anode non-equilibrium layer and a layer 'of the same thickness' in the undisturbed plasma, evaluated in terms of U_h, $\xi_{e\infty}$, $T_{e\infty}$ and U by means of equation (10).

Over all calculations, the electron temperature at the anode surface, T_{ew}, in the xenon plasma varies in a rather narrow range, between 4750 and 5735 K. The variations of T_{ew} in the mercury plasma are more significant although not dramatic, from 5480 to 7264 K. In both cases, the range of variation of T_{ew} is markedly narrower than the range of variation of the electron temperature in the undisturbed plasma, which is about 4600 K for the xenon plasma and about 3800 K for the mercury plasma. One can say that the coupling of the electron temperature in the vicinity of the anode surface to the operating conditions is rather weak, especially in the case of Xe, in contrast to what happens at the cathode (see discussion in [1, 9]).

The coefficient $\xi_{e\infty}$ varies between -0.77 and 0.74, i.e. is comparable to unity rather than small. Hence, the effect inverse to thermal diffusion may play an appreciable role, in contrast to what is frequently assumed.

The voltage drop U in the near-anode non-equilibrium layer in the mercury plasma is positive at $j = 10^7$ A m^{-2} and negative at $j = 10^8$ A m^{-2}; the voltage drop in the xenon plasma is negative in all cases. As the anode surface temperature increases, the near-anode voltage drop in the mercury plasma at $j = 10^7$ A m^{-2} decreases rather noticeably, from 1.49 to 0.65 V. In all the other cases, where U is negative, its variation with T_w is considerably smaller. The increase in the current density from 10^7 to 10^8 A m^{-2} at the same surface temperature causes a decrease in U between 2.4 and 3 V in the mercury plasma and of about 2 V in the xenon plasma. In other words, the current–voltage characteristic of the near-anode non-equilibrium layer at a constant T_w falls, in contrast to the characteristic of the near-cathode layer, which rises [9].

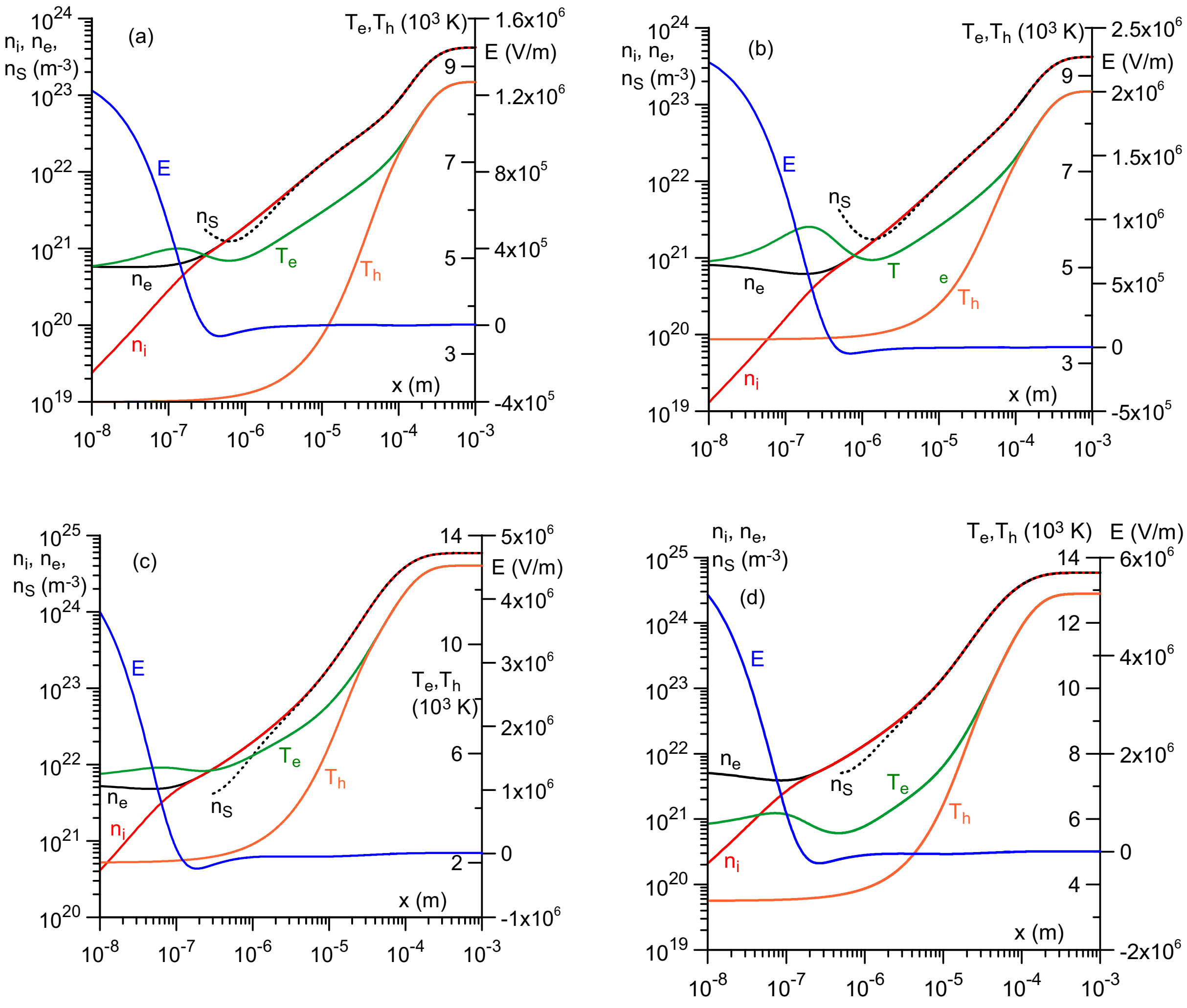

Figure 5. Distributions of parameters in the near-anode layer of the Xe plasma. $p_0 = 100$ bar. (*a*) $T_w = 2000$ K, $j = 10^7$ A m^{-2}. (*b*) $T_w = 3500$ K, $j = 10^7$ A m^{-2}. (*c*) $T_w = 2000$ K, $j = 10^8$ A m^{-2}. (*d*) $T_w = 3500$ K, $j = 10^8$ A m^{-2}.

As the plasma pressure increases at fixed j and T_w, the near-anode voltage increases, which is easily understandable: higher pressures reduce diffusion velocities of the charged particles, hence a higher power is needed to maintain the same current density at a higher pressure.

The anode heating voltage U_{h} in the xenon plasma is virtually independent of T_w, weakly decreases with an increase in the current density and weakly increases with an increase in the plasma pressure. However, these variations are quite small: in all the cases shown in table 1 U_{h} is between approximately 5.6 and 5.8 V, i.e. is virtually constant. In other words, the power input (energy flux) from the plasma to the anode is governed primarily by the arc current I and varies approximately proportionally to I, virtually without regard to the anode geometry, the current density and temperature distributions over the anode surface and the plasma pressure. U_{h} in the mercury plasma varies between approximately 6.7 and 9.4 V, i.e. its variations are more appreciable although not dramatic.

ΔU_{rad} is negative in all cases. In other words, the power radiated by the near-anode non-equilibrium layer is smaller than the power radiated by a layer 'of the same thickness' in the undisturbed plasma, which is a consequence of lower values of T_{e} in the near-anode layer. ΔU_{rad} is virtually independent of T_w and varies from -0.56 to -0.84 V in the mercury plasma and from -0.71 to -1.00 V in the xenon plasma.

According to equation (10), the anode heating voltage U_{h} is the sum of the three terms: the voltage equivalent of power transported by the electron current to the near-anode non-equilibrium layer from the undisturbed plasma, the voltage drop in the near-anode non-equilibrium layer and $-\Delta U_{\mathrm{rad}}$ the voltage equivalent of the decrease in the radiation losses. The first term, evaluated with the use of the data of table 1, is within the range 7.25 ± 0.6 V for mercury and 6.65 ± 0.9 V for xenon. The second term varies between approximately -3 and 2 V. The third term varies between 0.56 and 1.00 V. It follows that the main or even dominant contribution to the anode heating voltage is given by the power transported by the electron current to the near-anode non-equilibrium layer from the undisturbed plasma, contributions of the voltage drop in the near-anode non-equilibrium layer and of the decrease in the radiation losses are minor. This differs from what happens on high-pressure arc cathodes, where the near-cathode voltage in the diffuse mode, although not in the spot mode, represents

Table 1. Parameters of the near-anode non-equilibrium layers. The upper and lower numbers in each cell in the fourth and the following columns refer to the Hg and Xe arcs, respectively.

T_w (K)	j ($A\,m^{-2}$)	p_0 (bar)	T_{ew} (K)	$T_{e\infty}$ (K)	$\xi_{e\infty}$	U (V)	U_h (V)	ΔU_{rad} (V)
2000	10^7	100	6464 4750	8 380 8 676	0.57 −0.49	1.49 −1.00	8.94 5.75	−0.73 −0.75
2500	10^7	100	6445 4947	8 380 8 676	0.57 −0.49	1.18 −1.02	8.62 5.74	−0.72 −0.75
3000	10^7	100	6325 5104	8 380 8 676	0.57 −0.49	0.89 −1.02	8.32 5.73	−0.71 −0.75
3500	10^7	100	5480 5042	8 380 8 676	0.57 −0.49	0.65 −0.96	8.06 5.80	−0.70 −0.75
2000	10^8	100	7 264 5136	11 998 12 893	0.74 0.26	−1.52 −2.97	6.89 5.58	−0.56 −0.98
2500	10^8	100	7259 5363	11 998 12 893	0.74 0.26	−1.61 −2.95	6.80 5.60	−0.56 −0.99
3000	10^8	100	7 247 5571	11 998 12 893	0.74 0.26	−1.69 −2.94	6.72 5.62	−0.56 −0.99
3500	10^8	100	7089 5735	11 998 12 893	0.74 0.26	−1.76 −2.91	6.66 5.65	−0.56 −1.00
3000	10^7	50	6289 5377	8 591 9 094	0.60 0.16	0.10 −1.46	7.52 5.69	−0.62 −0.82
3000	10^7	200	6376 4817	8 192 8 331	0.55 −0.77	1.95 −0.63	9.44 5.82	−0.84 −0.71

the main component of the heating voltage and can be derived from the measured cathode heat losses (see discussion in [1]).

One of the conclusions of this section is that the modelling results support the general understanding of similarities and differences between plasma–cathode and plasma–anode interaction in high-pressure arc discharges as was discussed in [1].

4.2. Experimental results and comparison with the theory

Wherever a comparison is possible, the above-described modelling results conform to trends observed in the experiment. For example, a detailed experimental investigation of tungsten rod anodes in argon and other noble gases at pressures of 1–10 bar [30] indicated that the power input into the anode increases nearly proportionally to the arc current; the proportionality constant (the anode heating voltage) is independent of the electrically measured anode fall and scarcely dependent on the electrode dimensions; for a representative example of an argon plasma under the pressure of 2.6 bar to which table 1 of [30] refers, the anode heating voltage varies between 8.4 and 6.9 V while the arc current increases from 1 to 5 A. Clearly, these results are qualitatively similar to modelling results on U_h described in the preceding section. Unfortunately, a quantitative comparison of the modelling results of this work with the experimental data [30] is hardly possible, and not only because of essentially different pressure ranges. One should keep in mind, in particular, that the anode fall determined in [30] by means of electrostatic probe measurements involves not only the voltage drop in the near-anode non-equilibrium layer but also the voltage drop in the constriction region, which is not described by the present (1D) theory and is of the same order of magnitude as the voltage drop in the near-anode non-equilibrium layer.

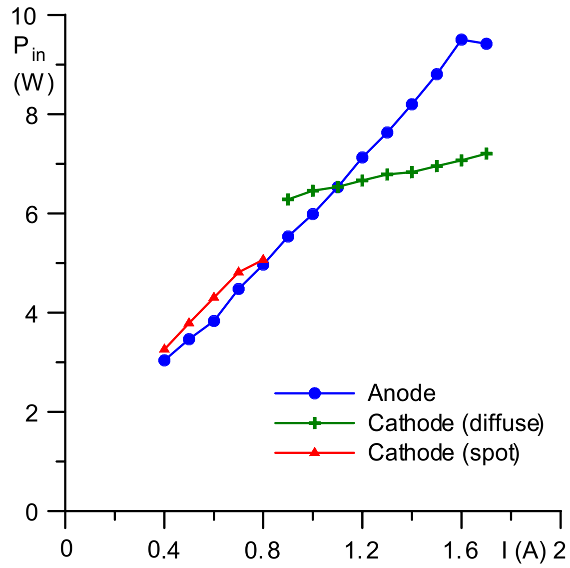

Figure 6. Power input P_{in} of the electrode determined experimentally in a very high-pressure Xe lamp for dc anode and dc cathode operation, as a function of the lamp current.

However, the modelling results can be compared with new experimental data obtained from the experiment described in section 3. Figure 6 shows the total heat load P_{in} for one of the electrodes when operated as the dc anode or the cathode. First consider the anode data. P_{in} varies linearly with I, except for the clear outlier at $I = 1.7$ A, the maximum current. An analysis of the respective CCD image shows that this current fully melted the spherical electrode front and even enlarged the size of the sphere, which falsified the value of P_{in} determined from the temperature profile. All other points are well described by a linear function with a slope $\mathrm{d}P_{\text{in}}/\mathrm{d}I = 5.4$ V and an offset of 0.7 W. This offset, however, is less certain than the good linearity in figure 6 suggests, because systematic errors in the experiment can shift all P_{in} values in the same way. For example, the axial optical distortion by the bulb (section 3) is a known problem because it directly affects the measured temperature gradients and is difficult to compensate with only two axial reference points available here (electrode tip and diameter step at 1.10 mm from the tip). Therefore, the offset might be wrong by about 0.5 W, most probably too high; we do not exclude even a true proportionality (zero offset) as suggested by other anode measurements [30, 31]. Given these provisos, our data imply an anode heating voltage U_{h} of about 5.5–6.0 V for anodes in a very high-pressure (about 100 bar) xenon plasma. This conforms well to the range of $U_{\text{h}} = 5.6$–5.8 V predicted by the modelling for the xenon plasma (table 1).

For comparison, figure 6 shows the cathode data also. Although of no direct interest for the anode theory of this work, the data are valuable because cathode measurements for these conditions have not been published before, to our knowledge. At low currents, $I \lesssim 0.8$ A, the cathode operates in the spot mode; at high currents, $I \gtrsim 0.9$ A, the cathode operates in the diffuse mode. Switching to the diffuse mode is accompanied by a noticeable increase in the power input; this feature is well known both from experiment and modelling (e.g. [1] and references therein). The $P_{\text{in}}(I)$ characteristic of the diffuse mode is much flatter than the characteristic of the spot mode and of the anode; the diffuse-cathode and anode curves cross near $I = 1.1$ A.

Reproducing these cathode data could be an interesting task for modellers. The required electrode geometry is described in section 3. The boundary condition at the (formal) electrode foot (2.0 mm from the tip) could be

$$T_{\text{foot}} = 300\, P_{\text{foot}} + 800 \tag{12}$$

(T_{foot} in K and P_{foot} the thermal power conducted into the feedthrough in W). This formula describes well the relation between the values of T_{foot} and P_{foot} that were determined, along with the P_{in} values shown in figure 6, from fitting the temperature profiles.

Another possible comparison between the theory and the experiment concerns distributions of near-electrode plasma radiances, which were extracted from the same bandpass-filtered CCD image as the electrode temperatures (figure 2). The near-anode radiances for several settings are shown in figure 7. Points have been obtained by measuring the spectral radiance w_{sr} (at 850 nm) in the centre of the arc, at increasing distance from the anode surface (curved line in figure 2). There are four sets of experimental data in figure 7. Three sets of data refer to the same arc current $I = 0.5$ A and three different values of the electrode temperature, $T_w = 2300$, 2400, 2900 K. (The operation at different electrode temperatures at the same current was achieved by creating suitable transient situations through current stepping.) The fourth set refers to $T_w = 2400$ K and $I = 1$ A. Lines represent w_{rad} the calculated radiative losses of electron energy; note that the

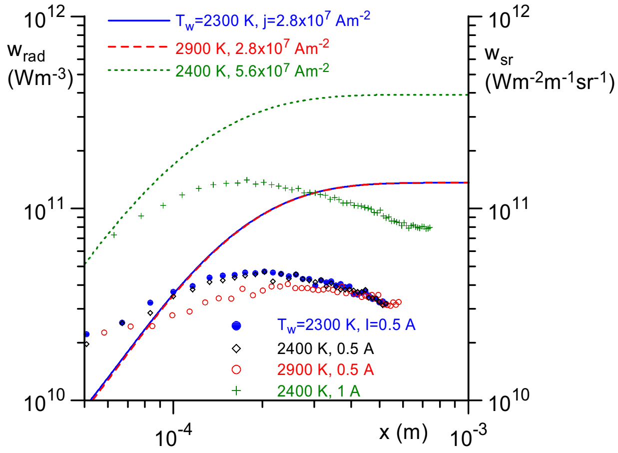

Figure 7. Points: measured spectral radiance in the near-anode layer of a very high-pressure xenon arc. Lines: calculated radiation power losses.

solid and the dashed lines are superimposed. The current density j values used in the simulations have been obtained by dividing the arc current (0.5 or 1.0 A) by the attachment area which was estimated from the apparent spot diameter of about 150 μm seen in the images. The plasma pressure in the simulations was assumed equal to 100 bar. The data are plotted on distances from the anode surface exceeding 50 μm, since the experimental data are likely not to be very reliable at smaller distances.

The theoretical data, being obtained by means of a 1D model which does not take into account the expansion of the arc from the anode into the plasma seen in figure 2, are applicable at distances from the anode surface not exceeding, say, 150 μm, which is the above-mentioned diameter of the anode attachment. Therefore, the modelling can be expected to correctly describe the deviations from LTE, since they are localized at distances from the anode surface below 100 μm as seen in figure 5. On the other hand, it is not surprising that the theoretical curves are monotonic while the experimental data show a radiance maximum at a distance from the anode surface somewhere around 200–300 μm, originating presumably in the above-mentioned expansion of the arc into the plasma.

The experimental data and modelling refer to different quantities: the spectral radiance w_{sr} represents the energy radiated by a unit area of the arc in a unit spectral interval per unit time per steradian, while w_{rad} represents radiative losses of electron energy per unit time and volume, i.e. the net emission coefficient of the plasma (e.g. [32, 33]) integrated over the solid angle. Therefore, the same order of magnitude of the modelling and experimental data does not have much significance and one should focus on qualitative factors, such as effects of the temperature of the anode surface and the arc current.

According to the experiment, the effect of the anode temperature on the radiation emission is weak. The same trend is seen in the modelling. The experiment shows that an increase in the arc current by a factor of 2 (from 0.5 to 1.0 A) leads to an increase in the centre-of-arc radiance by about a factor of 3. It seems that an increased current density could be the only plausible explanation of this increase and indeed doubling of the current density in the modelling, from 2.8×10^7 to 5.6×10^7 A m^{-2}, boosts the radiation strongly, by about a factor of 4. This suggests that a change in the total current in the experiment really means a change in the current density on the anode, not so much of the area of the arc attachment to the anode, since the light emission would not change that much in the latter case.

This section may be summarized as follows. Very high-pressure arc discharges represent a difficult object for experimental investigation. The experiments described in section 3 provided at least some basic quantitative data, and these data conform reasonably well to the modelling.

5. Conclusions

The numerical model [9], which was used previously for a simulation of near-cathode plasma layers, is employed for the investigation of near-anode layers of very high-pressure arcs in mercury and xenon. The simulation results support the general understanding of similarities and differences between plasma–cathode and plasma–anode interaction in high-pressure arc discharges summarized in [1].

The power injected by the plasma into the anode tip is found to be governed primarily by the arc current and to vary approximately proportionally with the current, effects of the anode geometry, the form of the arc attachment, the conditions of cooling of the anode and the plasma pressure being minor. The anode heating voltage U_h may be represented as a sum of the three terms: the voltage equivalent of the power transported by the electron current to the near-anode non-equilibrium layer from the undisturbed plasma, the voltage drop in the near-anode non-equilibrium layer and the voltage equivalent of the decrease in the radiation losses. The first term is within the range 7.25 ± 0.6 V for mercury and 6.65 ± 0.9 V for xenon. The second term varies between approximately -3 and 2 V. The third term varies between 0.56 and 1.00 V. It follows that the main or even dominant contribution to anode heating is given by the power transported by the electron current to the near-anode non-equilibrium layer from the undisturbed plasma.

A new experimental investigation of the plasma–anode interaction in very high-pressure xenon arcs is performed by means of recording the spectral radiance from the electrodes and the near-anode plasma. The resulting axial surface temperature profiles were used to derive the power input P_{in} from the plasma to the electrodes. The results agree well with those of the simulations. The conclusion that the power input from the plasma to the anode tip is governed primarily by the arc current I and varies approximately proportionally to I and that the anode heating voltage is unrelated to the near-anode voltage conforms also to results of experiments [30], performed in noble gases at pressures of 1–10 bar.

According to both the modelling and the experiment, the effect of the anode temperature on the radiation emission from the near-anode plasma is weak. The experimental observation that an increase in the arc current by a factor of 2 (from 0.5 to 1.0 A) leads to an increase in the centre-of-arc radiance by about a factor of 3 may be explained by assuming that a change in the arc current in the experiment really means a change in the current density on the anode, not so much of the area of the arc attachment to the anode.

Acknowledgments

The work at UMa was supported by the project PPCDT/FIS/60526/2004 *Modes of current transfer to cathodes of high-pressure arc discharges and their stability* of FCT, POCI 2010 and FEDER and by the project *Centro de Ciências Matemáticas* of FCT, POCTI-219 and FEDER. One of the authors (UH) thanks the Business Center Automotive, Aachen, of Philips Lighting for providing the experimental lamps.

References

[1] Benilov M S 2008 *J. Phys. D: Appl. Phys.* **41** 144001
[2] Amakawa T, Jenista J, Heberlein J V R and Pfender E 1998 *J. Phys. D: Appl. Phys.* **31** 2826–34
[3] Haidar J 1999 *J. Phys. D: Appl. Phys.* **32** 263–72
[4] Lago F, Gonzalez J J, Freton P and Gleizes A 2004 *J. Phys. D: Appl. Phys.* **37** 883–97
[5] Flesch P and Neiger M 2005 *J. Phys. D: Appl. Phys.* **38** 3098–111
[6] Bini R, Monno M and Boulos M I 2006 *J. Phys. D: Appl. Phys.* **39** 3253–66
[7] Lowke J J and Tanaka M 2006 *J. Phys. D: Appl. Phys.* **39** 3634–43
[8] Lenef A, Dabringhausen L and Redwitz M 2004 *Proc. 10th Int. Symp. on the Science and Technology of Light Sources (Toulouse, July 2004)* ed G Zissis (Bristol: Institute of Physics Publishing) pp 429–30
[9] Almeida N A, Benilov M S and Naidis G V 2008 *J. Phys. D: Appl. Phys.* **41** 245201
[10] Mentel J, Luhmann J and Nandelstädt D 2000 *Industry Applications Conf. (Rome, 2000)* (Conference Record of the 2000 IEEE) vol 5 pp 3293–300
[11] Adler H G 2000 *Industry Applications Conf. (Rome, 2000)* (Conference Record of the 2000 IEEE) vol 5 pp 3309–13
[12] Dinulescu H A and Pfender E 1980 *J. Appl. Phys.* **51** 3149–57
[13] Nazarenko I P and Panevin I G 1989 *Contrib. Plasma Phys.* **29** 251–61
[14] Tanaka M, Ushio M and Wu C S 1999 *J. Phys. D: Appl. Phys.* **32** 605–11
[15] Zhdanov V M 2002 *Transport Phenomena in Multicomponent Plasma* (London and New York: Taylor and Francis)
[16] Rat V, Murphy A B, Aubreton J, Elchinger M F and Fauchais P 2008 *J. Phys. D: Appl. Phys.* **41** 183001
[17] Luhmann J, Lichtenberg S, Langenscheidt O, Benilov M S and Mentel J 2002 *J. Phys. D: Appl. Phys.* **35** 1631–8
[18] Bauer A and Schultz P 1954 *Z. Phys.* **130** 197–211
[19] Benilov M S and Naidis G V 1998 *Phys. Rev.* E **57** 2230–41
[20] Duman E L *et al* 1982 *Preprint of the Kurchatov Institute of Atomic Energy No. 3532/12* (Moscow: Institute for Atomic Energy) (in Russian)
[21] Smirnov B M 2001 *Phys. Usp.* **44** 221–54
[22] Itikawa Y (ed) 2000 *Photon and Electron Interactions with Atoms, Molecules and Ions. Subvolume A Interactions of Photons and Electrons with Atoms* (*Numerical Data and Functional Relationships in Science and Technology* vol 17A) (Berlin: Springer)

[23] Phelps A V 2008 http://jilawww.colorado.edu/~avp/collision_data/electronneutral/ELECTRON.TXT, last modified 24-Jun-2008
[24] Vargaftik N B and Vasilevskaya Y D 1980 *J. Eng. Phys. Thermophys.* **39** 1217–22
[25] Tawara H and Kato T 1987 *At. Data Nucl. Data Tables* **36** 167
[26] Radtke R and Kettlitz M 1992 *Plasma Sources Sci. Technol.* **1** 274–9
[27] de Vos J C 1954 *Physica* **20** 690–712
[28] Nemchinskii V A and Perets L N 1977 *Sov. Phys.—Tech. Phys.* **22** 1083–7
[29] Nemchinsky V A 2005 *J. Phys. D: Appl. Phys.* **38** 4082–9
[30] Redwitz M, Dabringhausen L, Lichtenberg S, Langenscheidt O, Heberlein J and Mentel J 2006 *J. Phys. D: Appl. Phys.* **39** 2160–79
[31] Hechtfischer U, Krücken T and Mönch H 2003 Thermische Eigenschaften von Elektroden in Hochdruckplasmalampen *Final Report of BMBF Project 13N7766* (Aachen, Germany: Philips Research)
[32] Lowke J J 1970 *J. Appl. Phys.* **41** 2588–600
[33] Gleizes A, Gonzalez J J and Freton P 2005 *J. Phys. D: Appl. Phys.* **38** R153–83